ChemPubSoc Europe

DOI: 10.1002/chem.201904170

CHEMISTRY A European Journal Full Paper

Clathrates |*Hot Paper*|

In-Cage Interactions in the Clathrate Superconductor Sr_8Si_{46}

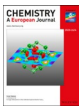

Julia-Maria Hübner, Yurii Prots, Walter Schnelle, Matej Bobnar, Markus König, Michael Baitinger, Paul Simon, Wilder Carrillo-Cabrera, Alim Ormeci, Eteri Svanidze, Yuri Grin, and Ulrich Schwarz*[a]

Abstract: The clathrate I superconductor Sr_8Si_{46} is obtained under high-pressure high-temperature conditions, at 5 GPa and temperatures in the range of 1273 to 1373 K. At ambient pressure, the compound decomposes upon heating at $T = 796(5)$ K into Si and $SrSi_2$. The crystal structure of the clathrate is isotypic to that of Na_8Si_{46}. Chemical bonding analysis reveals conventional covalent bonding within the silicon network as well as additional multi-atomic interactions between Sr and Si within the framework cages. Physical measurements indicate a bulk BCS type II superconducting state below $T_c = 3.8(3)$ K.

Introduction

Polar intermetallic compounds constitute a class of metal-rich solids often characterized by definite chemical composition. The more electropositive metal, usually an alkali, alkaline-earth or rare-earth metal, transfers its valence electrons to the more electronegative constituent, often a post-transition element of the p-block, yielding polyanionic species, which frequently involve covalent bonds. In three-dimensional anionic frameworks, the cations are often located in extended cavities, thus forming cage-like coordination environments. Some scaffold structures can adapt to different electron counts and bonding situations. Besides classical 8-*N* scenarios, silicon compounds may also form metallic Zintl phases[1,2] hosting excess electrons. Their role in chemical bonding is still under discussion, but a recent study on $MgSi_5$ evidences that they may be used for additional (nonionic) metal–framework interactions within the cages.[3]

Within the extensive family of cage compounds, clathrates represent a subset of scaffold structures with a broad spectrum of interesting physical properties, such as superconductivity[4] and high charge carrier mobility in combination with glass-like thermal conductivity,[5] suitable for thermoelectric applications. The type I clathrates (Figure 1), based on Si and Ge, have been widely studied, for example, $M_{8-x}Tt_{46}$ (M = Na, K, Rb, Cs, Ba; Tt = Si, Ge).[6–24] A great deal of attention has been paid to the binary barium-containing phase $Ba_{8-x}Si_{46}$[11–17] and its ternary derivatives $Ba_8Z_xSi_{46-x}$ (Z = Al, Ni, Cu, Zn, Ga, Ge, Rh, Pd, Ag, Cd, Pt, Au).[25–29] In contrast, only a small number of ternary strontium compounds have been reported,[15,30–32] and the corresponding binary strontium clathrate of silicon remained experimentally inaccessible so far.[33] Moreover, computational studies

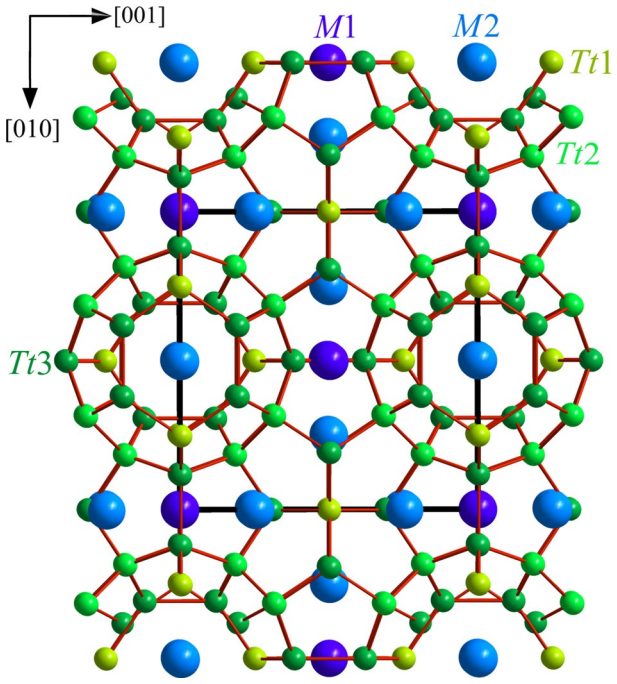

Figure 1. An idealized crystal structure of type-I clathrate. Metal atoms *M* are shown in blue while the network atoms *Tt* are marked in green. Red lines denote shortest nearest neighbor distances, black lines show the unit cell.

[a] *J.-M. Hübner, Dr. Y. Prots, Dr. W. Schnelle, Dr. M. Bobnar, Dr. M. König, Dr. M. Baitinger, Dr. P. Simon, Dr. W. Carrillo-Cabrera, Dr. A. Ormeci, Dr. E. Svanidze, Prof. Y. Grin, Dr. U. Schwarz*
Chemische Metallkunde
Max-Planck-Institut für Chemische Physik fester Stoffe
Nöthnitzer Straße 40, 01187 Dresden (Germany)
E-mail: schwarz@cpfs.mpg.de

Supporting information and the ORCID identification number(s) for the author(s) of this article can be found under: https://doi.org/10.1002/chem.201904170.

ruled out the stability of Sr_8Si_{46} in the pressure range from 0.1 MPa (ambient) up to 15 GPa.[34,35] We obtain this clathrate by high-pressure high-temperature synthesis at 5 GPa and at temperatures between 1273 and 1373 K. In this work, we report the crystal structure, chemical bonding and superconductivity of the binary strontium clathrate Sr_8Si_{46}.

Results and Discussion

Besides the new clathrate Sr_8Si_{46}, the crude reaction products contain about 6% residual silicon. The composition is $Sr_{8.15(3)}Si_{45.85(3)}$ based on energy-dispersive X-ray spectroscopy and $Sr_{8.26(1)}Si_{45.74(1)}$ based on wavelength-dispersive X-ray spectroscopy, which is both in satisfactory agreement with the result of the structure refinement. The pattern obtained by powder X-ray diffraction of Sr_8Si_{46} is fully indexed in the cubic system using $Pm\bar{3}n$ space group with $a = 10.2508(5)$ Å. Reflection intensities indicate that the compound adopts a clathrate I motif and is thus isotypic to Na_8Si_{46}.[6] Differential scanning calorimetry measurements at ambient pressure reveal the decomposition (Figure 2) of Sr_8Si_{46} at $T = 796(5)$ K into (*t*/12) $SrSi_2$[36] and Si.[37]

Given the metastable nature of Sr_8Si_{46}, a comparison of the unit cell volume with those of clathrates, which are stable at ambient pressure, is shown in Figure 3. The volume of the $Ba_xSr_ySi_{46}$ mixed phase decreases significantly upon increased strontium substitution ratio. The same trend is observed for the Ba_xSi_{46} defect phase. Here, the volume becomes smaller with decreasing occupancy of the Ba positions. In line with the requirement of high pressure for the synthesis of the pure strontium compound, the minimum volumes of Ba_xSi_{46} and $Ba_xSr_ySi_{46}$ phases are slightly larger than that of Sr_8Si_{46}.

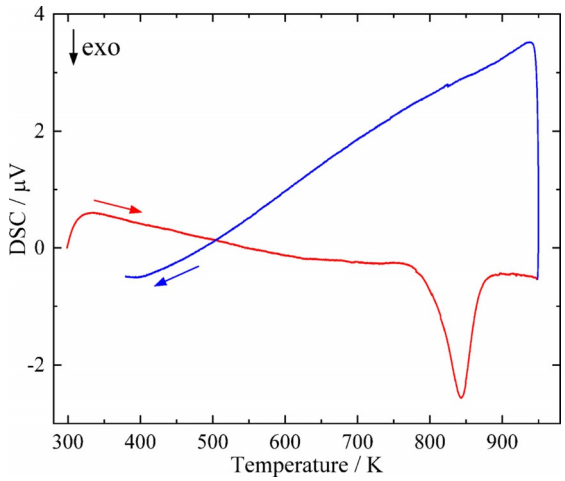

Figure 2. Differential scanning calorimetry measurement of Sr_8Si_{46} taken upon heating (red curve) and cooling (blue curve) in the range $300\ K \leq T \leq 950\ K$ with a heating rate of 10 K min^{-1} at ambient pressure.

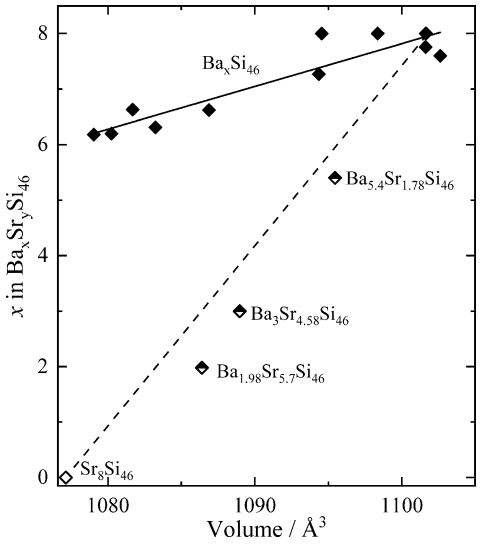

Figure 3. Unit cell volume *V* of Sr_8Si_{46} along with to the related Ba_xSi_{46}[11–17] and $Ba_xSr_ySi_{46}$[30] barium phases. The corresponding error bars are smaller than the chosen symbol size. The solid line represents a fit to the data for Ba_xSi_{46}, the dashed line indicates a volume dependence according to Vegard's law.

For a more detailed characterization of the new clathrate, the atomic arrangement of Sr_8Si_{46} was investigated by means of single crystal X-ray diffraction. The refinements result in the residual $R = 0.048$ ($F > 4\sigma(F)$, Table 1), evidencing good sample quality and sound agreement of the selected structure model with the measured data. For both the strontium and the silicon sites, no indication for partial occupation is found within the standard deviations, giving the chemical composition Sr_8Si_{46}. The atomic displacement parameters (Table 2) show similar values, except for Sr2. The introduction of a split model for Sr2 did not improve the residuals. Moreover, an apparently slightly larger atomic displacement is generally observed for the oversized 24-atom cages.[38] Therefore, we have no experimental

Table 1. Single crystal XRD data for Sr_8Si_{46}.

Composition	Sr_8Si_{46}
space group, Pearson symbol	$Pm\bar{3}n$ (No. 223), *cP*54
unit cell parameter	
a [Å]	10.2508(5)
V [Å^3]	1077.1(2)
formula units *Z*	1
diffractometer	Rigaku Saturn724+, CCD detector, graphite monochromator, Mo $K\alpha$ radiation, $\lambda = 0.71073$ Å
reflections collected/independent within $F > 4\sigma(F)$	8497/372
measurement range	$-15 \leq h \leq 15$, $-15 \leq k \leq 7$, $-15 \leq l \leq 13$
residuals and GOF	$R = 0.048$, $wR = 0.053$, GOF = 1.07

Table 2. Atomic coordinates and displacement parameters for Sr_8Si_{46}.

Atom	Site	*x/a*	*y/b*	*z/c*	B_{eq}
Sr1	2*a*	0	0	0	1.06(3)
Sr2	6*d*	1/4	1/2	0	1.64(3)
Si1	6*c*	1/4	0	1/2	0.89(6)
Si2	16*i*	0.1843(2)	*x*	*x*	0.90(3)
Si3	24*k*	0	0.3067(2)	0.1191(2)	0.90(4)

evidence for defects or vacancies in Sr_8Si_{46}, in contrast to Ba_xSi_{46}.[11–17]

In order to investigate how the incorporation of guest atoms of similar charge but different size affects the resulting framework, the shortest host–guest distances in the small and large cages are discussed. The calculated distances *d*(*M*–Si) for *M* = Sr and *M* = Ba differ by less than 1% by using the atomic radii.[40] The shortest observed distances in the small cages *d*(*M*1–Si2) differ by 3.3% and the distances *d*(*M*2–Si3) in the large cage change by 1.1% [see Table 3 for Sr_8Si_{46} and *d*(Ba1–Si2) = 3.3129 Å and *d*(Ba2–Si3) = 3.4973 Å[16]]. Simultaneously, the shift of the Si2 atoms causes a decrease of the [111] oriented distance *d*(Si2–Si2) of 0.5%.

Table 3. Selected interatomic distances (in Å) of Sr_8Si_{46}.

Atom	Distance	Atom	Distance
Sr1–8 Si2	3.274(1)	Si1–4 Si3	2.392(2)
Sr1–12 Si3	3.373(2)	Si2–1 Si2	2.329(2)
Sr2–4 Si1	3.6242(1)	Si2–3 Si3	2.365(2)
Sr2–8 Si2	3.806(2)	Si3–1 Si3	2.444(3)
Sr2–8 Si3	3.462(1)		

In order to address the microstructure of Sr_8Si_{46}, high-resolution transmission electron microscopy (HR-TEM) studies were carried out. Oriented focused ion beam (FIB) cross-sections, perpendicular to the [010] and [110] directions, were cut and thinned (Figure 4). The crystallites of Sr_8Si_{46} show preferred cleavage along the {100} planes. HR-TEM images (Figure 5) give no indication for deviation from cubic symmetry, defects on the cage sites or the formation of a superstructure.

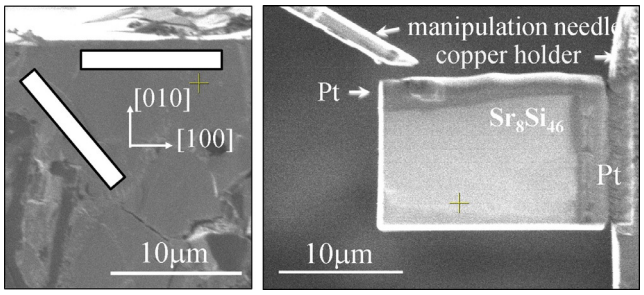

Figure 4. Left: Structured illumination microscopy (SIM) image of the cleaved surface of a Sr_8Si_{46} sample with Si inclusions (dark gray). White bars with black frames show the positions for two focused-ion beam cuts of a Sr_8Si_{46} crystallite. Right: SIM image of an extracted [010] FIB cut.

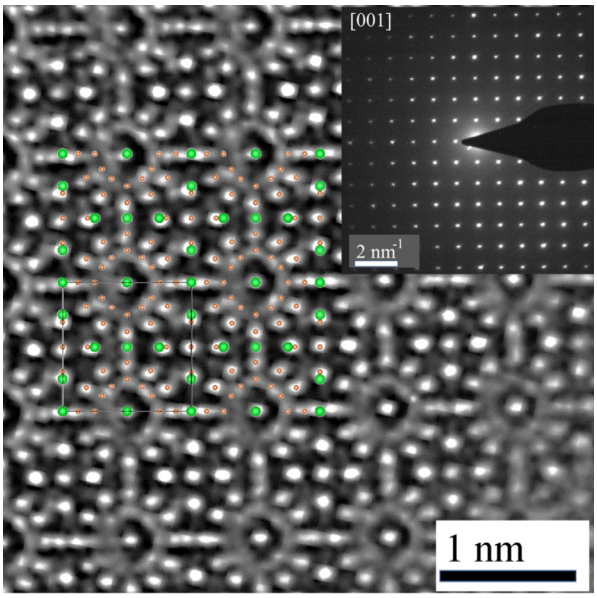

Figure 5. Spherical-aberration-corrected HR-TEM image of the [001] zone of Sr_8Si_{46}. The Si-cage is clearly imaged as well as the host Sr positions at the corners of the squares. The regular ordering reveals full occupation of the metal sites. Atomic positions are indicated by colored dots. The inset displays an electron diffraction pattern recorded from a several microns sized area of interest and shows a regular cubic lattice without any indication for superstructure formation involving cell doubling.

For verifying the local structure of the clathrate network, magic-angle spinning ^{29}Si NMR spectra of Sr_8Si_{46} are recorded (Figure 6, black line). These show three strongly shifted signals, which clearly point to the presence of a Knight shift and, thus, to a metallic behavior of Sr_8Si_{46}. Signals are centered at 2387(5) ppm, 1726(5) ppm, and 1065(5) ppm. The relative intensities of 5.5(5):29(1):11.5(7) readily identify these lines as belonging to Si residing at the 6*c*, 24*k*, and 16*i* positions, respectively. The reasons for the deviation from the expected ratio of 6:24:16 are most likely experimental imperfections, such as different spin-spin and spin-lattice relaxation times for the three

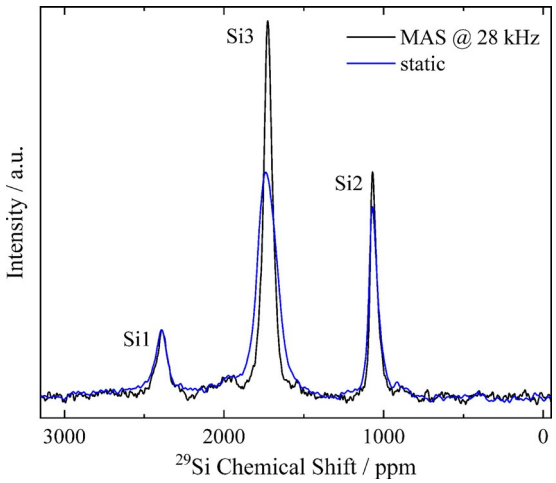

Figure 6. The ^{29}Si NMR spectrum of Sr_8Si_{46} at room temperature, spinning at 28 kHz at magic angle (black) and static measurement (blue).

sites and the limited observation window, which was centered on the middle line. The static spectrum of the same sample (Figure 6, blue line) shows almost no broadening of the signals at 2387 ppm and 1065 ppm, whereas the line at 1726 ppm is noticeably wider. Moreover, the asymmetric line shape points at the presence of a magnetic shift anisotropy in accordance with the low symmetry of the 24*k* site. Although the experimental line intensity ratios hamper a conclusive statement concerning defects, the sharpness of the signals suggest the absence of disorder in the structure and, thus, points to the full occupation of the cages by Sr atoms. This is in contrast to Ba_xSi_{46} clathrates.[15] The large ^{29}Si Knight shifts (spanning between 1000 ppm and 2400 ppm) of Ba and Sr filled clathrates-I indicate to a relatively large density of Si states at the Fermi level, which is a promising prerequisite for superconductivity. Accordingly, non-superconducting Na_8Si_{46} shows lower Knight shifts in the range from 600 to 850 ppm.[39]

The crystal structures and compositions of most strontium silicides can be successfully described within the Zintl concept. The (formal) electron transfer from strontium onto the silicon substructure yields additional electrons which are used for satisfying the 8-*N* Pearson rule for covalent framework, for example, $Sr^{2+}[(3b)Si^{1-}]_2\times 0\,e^-$.[41] Moreover, binary germanium clathrates (in particular those of the alkali metals) usually realize an electron precise balance by forming defects in the anionic framework, which localize the excess electrons in lone pairs, for example, in $K_8Ge_{44\square 2}$. In contrast, Sr_8Si_{46} and its barium analogue Ba_8Si_{46} reveal excess electrons according to the Zintl balance $[M^{2+}]_8[(4b)Si^0]_{46}\times 16\,e^-$ (M = Sr, Ba). This phenomenon is attributed to the lower stability of framework vacancies for silicon in comparison to germanium.[42]

The calculated electronic density of states for Sr_8Si_{46} (Figure 7, top) contains two large regions. The section below the Fermi level is dominated by *s* and *p* states of silicon with small contributions of the *s* and *d* states of strontium. Above the pseudo-gap, we find larger contributions of strontium *d* states. The Fermi energy is located above a pseudo-gap implying the occupation of antibonding states similar to the situation in Ba-containing clathrates.[43] In accordance with substantial charge transfer from strontium to the silicon framework, the analysis within the QTAIM approach (quantum theory of atoms in molecules[44]) reveals effective positive charges of +1.49 and +1.34 for Sr1 and Sr2, respectively (Figure 7, bottom). The values are similar to those of +1.33 to +1.51 in $SrGe_{6-x}$[45] and +1.51 and 1.54 in the clathrate $Sr_8Al_6Si_{40}$[31] as well as charges between 1.2 and 1.54 in related strontium compounds.[46–48] For Ba–Ge clathrates, charges of +1.1 and +1.4 are found.[43]

The charge of the silicon atoms vary from +0.22 for Si1 to −0.32 for Si2 and −0.90 for Si3. A similar differentiation was found for the network species in the Ba–Ge clathrates. The almost perfectly spherical shapes of the strontium QTAIM atoms in Sr_8Si_{46} indicate mostly ionic interactions between guest and network atoms, similar to Ba atoms in Ge clathrates.[43] The shapes of the basins around the silicon atoms have several plane faces, which are characteristic for covalent interactions, especially between homoatomic species.

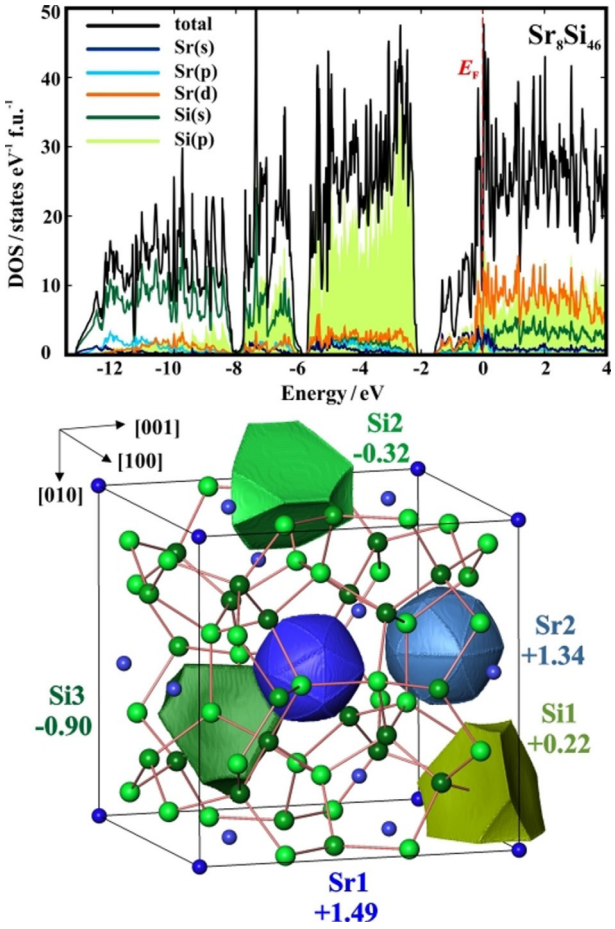

Figure 7. Top: Calculated total electronic density of states of Sr_8Si_{46} and selected atomic contributions of Sr and Si. Bottom: Shapes of the QTAIM atoms[44] and calculated effective charges.

The covalent bonding between the silicon atoms is clearly confirmed be the topological analysis of ELI-D. The distribution in Sr_8Si_{46} (Figure 8, top) reveals the characteristic picture of four-bonded silicon atoms in the framework. The maxima of ELI-D, visualized by the isosurface with ELI-D = 1.566, are located on or close to the bond lines between neighboring silicon atoms (Figure 8, top). In this representation, no dedicated ELI-D features exist between Sr and Si. Thus, the role of the electrons in states above the pseudo-gap-like structure in the electronic DOS is evaluated by the partial ELI-D (pELI-D) approach.[49] The ELI-D is calculated for states with energies between −1.6 eV (local minimum in the DOS below E_F) and the Fermi level. The integration of the electronic DOS in the window between −1.6 eV and the Fermi level yields 16 electrons per formula unit, which is in good agreement with the number of excess electrons in the Zintl balance.

The contributions of pELI-D for this energy window are found within the coordination polyhedra of Sr1 and Sr2, that is, in the framework cages (Figure 8, bottom). These local maxima of pELI-D reveal multi-atomic Sr–Si interactions within the large cavity of the framework around Sr2 and less pronounced ones in the vicinity of Sr1 (in-cage bonding).

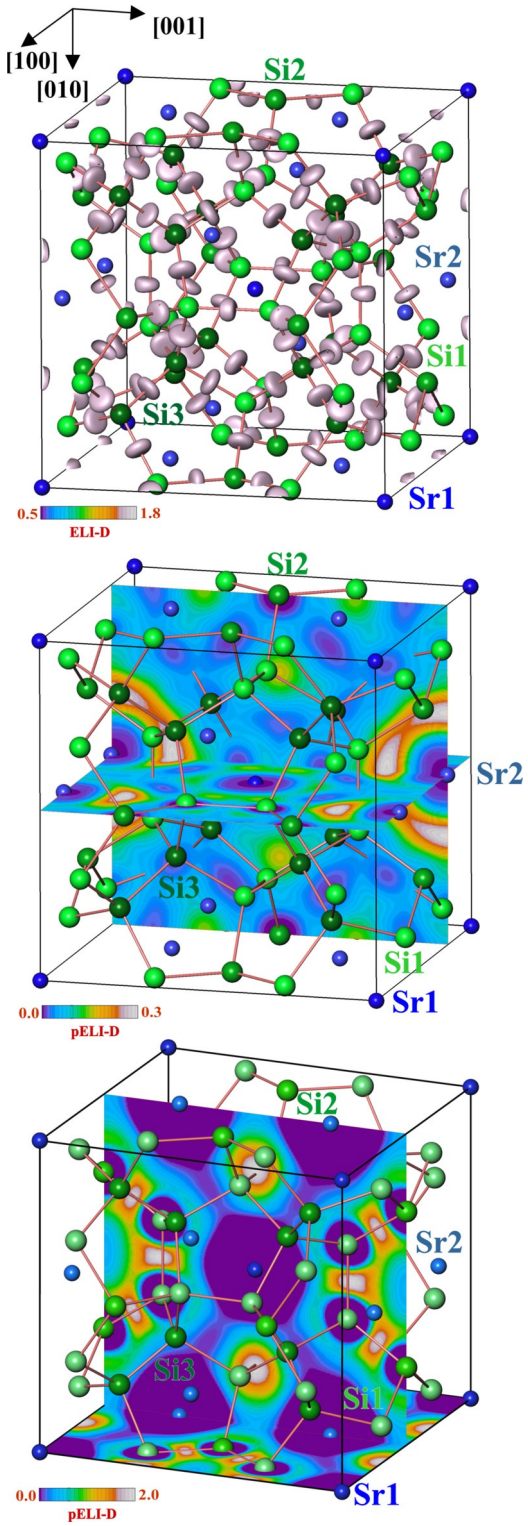

Figure 8. Top: Isosurface of ELI-D = 1.566 revealing the covalent Si–Si bonds within the anionic framework. Middle: Distribution of partial ELI-D in the (020) and (400) planes for the energy window $-1.6\ \text{eV} \leq E \leq E_F$ visualizing the atomic interactions within the Sr1 and Sr2 environments, respectively. Bottom: Partial ELI-D in the (010) and the (020) plane for the energy window $-5.7\ \text{eV} \leq E \leq -2.1\ \text{eV}$ showing the bonding in the silicon framework.

A similar scenario was recently found for yttrium hexaboride (CaB_6 type crystal structure) with a boron framework embedding the yttrium atoms in large cavities. In comparison with the calcium prototype, the yttrium compound has one excess electron per formula unit, and the analysis of the according pELI-D reveals the multi-atomic interactions within the coordination sphere of yttrium.[50]

Following this way of analysis, the electrons below the pseudo-gap should contribute mainly to the regions of the Si–Si bonding. Indeed, the electrons from the energy window between −5.7 and −2.1 eV yield the pELI-D maxima in the Si–Si bonds regions within the framework (Figure 8 bottom).

The magnetic susceptibility χ of Sr_8Si_{46} reveals a diamagnetic transition with a critical temperature $T_c = 2.8(3)$ K (Figure 9).

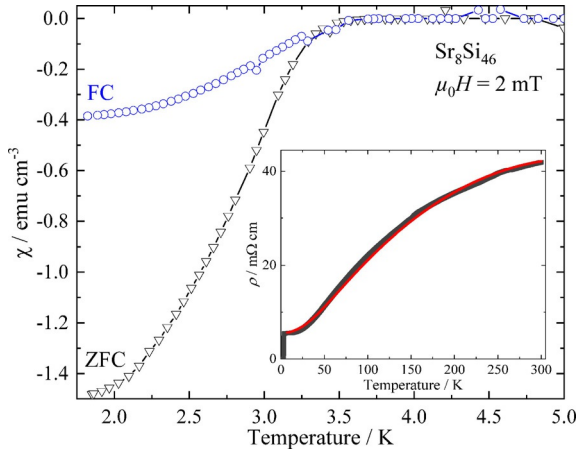

Figure 9. Magnetic susceptibility χ of Sr_8Si_{46} measured in an external field of 2 mT at temperatures between 1.8 and 5 K. Inset: Temperature-dependent electrical resistivity ρ at zero-field. The solid red line denotes the fit of a Bloch–Grüneisen equation to the experimental data.

The Meissner volume fraction exceeds 1 (without correction for demagnetization effects), implying bulk superconductivity. The large ratio χ_{ZFC}/χ_{FC} indicates type II superconductivity.

The electrical resistivity at ambient temperature ρ(T) (Figure 9, inset) amounts to 42 mΩ cm, which is in line with the values reported for other clathrates.[51–54] The residual resistance ratio is $\rho_{293K}/\rho_{4K} = 7.7$, implying a good sample quality. The zero-field electrical resistivity shows a positive slope in the normal conducting state, pointing towards metallic behavior. Considering the Mattheisen rule, the normal state resistivity is well-described within the Bloch–Grüneisen model.[55–57] The best fit is achieved with the residual resistivity $\rho_0 =$ 5495(17) μΩ cm, the electron-phonon coupling constant $A =$ 924(2) μΩ cm K, the Debye temperature $\theta_D = 281(2)$ K, and the coefficient of the cubic term $k = 0.345(2)$ μΩ cm K^{-2}. The reason for the high resistivity values is probably a semiconducting contribution of insulating phases located at the grain boundaries, for example, Si or SiO_2, as observed in a similar manner for polycrystalline phases of the Ba_xSi_{46} clathrate.[15,58] In zero-field, the resistivity drops with an onset $T_c = 3.8(3)$ K, confirming the transition into the superconducting state. At $T_c = 2.3(3)$ K, zero resistivity is reached.

The specific heat C_p(T) of Sr_8Si_{46} (Figure 10, top) shows a transition at $T_{c,mid} = 3.3(3)$ K in $\mu_0 H = 0$. In the normal conduct-

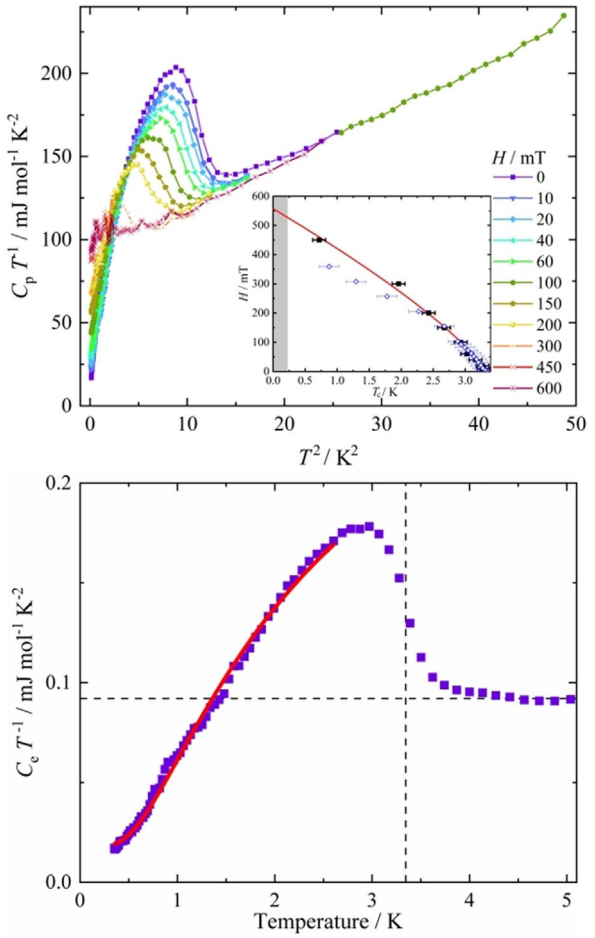

Figure 10. Top: Specific heat capacity of Sr_8Si_{46} in different magnetic fields. Inset: Phase diagram with the dependency of the critical temperature T_c of Sr_8Si_{46} on the magnetic field. Black symbols show data points used for the fit, blue ones indicate an independent reference measurement of a second sample. Bottom: Electronic specific heat of Sr_8Si_{46}, the red line is denoting a fit by the BCS equation.

ing state at $\mu_0 H = 0$ T, the data are sufficiently described by the standard ansatz $C_p(T) = \gamma_N T + \beta T^3$, with $\gamma_N T$ being the Sommerfeld electronic heat and βT^3 referring to the first term of the harmonic lattice approximation of the phonon contribution.[55] The best fit was achieved with $\gamma_N = 88.7(7)$ mJ mol^{-1} K^{-2} and $\beta = 2.87(2)$ mJ mol^{-1} K^{-2}. From β, the Debye temperature $\theta_D = 332(2)$ K was calculated.[55,56] The strength of the electron–phonon coupling according to McMillan's formula[59] amounts to $0.50 \le \lambda_{e-p} \le 0.60$ assuming a value for the screened Coulomb repulsive potential $0.1 \le \mu^* \le 0.15$, pointing towards Sr_8Si_{46} being a weakly coupled superconductor.

The critical temperature T_c of Sr_8Si_{46}, taken from the first derivative of the specific heat $C_p(T)$, was plotted against the applied magnetic field (Figure 10, top, inset). The estimate of the upper critical field by the so-called Werthamer–Helfand–Hohenberg (WHH) extrapolation[60] results in $\mu_0 H_{c2} = 550(10)$ mT. The value of the critical field from the exponential fit gives $H_c = 557(10)$ mT, being in good accordance with the WHH value.

The electronic specific heat C_e is obtained by subtraction of the phonon contribution (Figure 10, bottom). The electronic contribution is well-described by the Bardeen–Cooper–Schrieffer (BCS) expression.[55] A least-squares fit yields $\gamma_0 = 0.018(1)$ mJ mol^{-1} K^{-2} and the energy gap $\Delta_0 = 0.17(2)$ meV $= 2\,k_B T$ at the Fermi level. This gives $2\Delta_0 k_B^{-1} T_c^{-1} = 2.46$, a value slightly below the BCS value of 3.52.[55]

Conclusions

We have synthesized the previously inaccessible type I clathrate Sr_8Si_{46} at 5 GPa and at temperatures between 1273 K and 1373 K. The atomic arrangement is isotypic to that of Na_8Si_{46} and the computed charge transfer from strontium to silicon is in line with the electronegativity difference of the constituting elements. Within the three-dimensional silicon framework, the atomic interactions are realized as covalent two-atomic bonds. Additionally, the valence electrons of strontium are involved in unique multi-atomic Sr–Si interactions within the framework cavities hosting the cations (in-cage bonds). The strontium clathrate undergoes a phase transition into a bulk BCS type II superconducting state below $T_c = 3.8(3)$ K, as indicated by measurements of magnetic susceptibility, electrical resistivity, and specific heat.

Experimental Section

Sample handling, except for high-pressure synthesis itself, was performed in argon-filled glove boxes (MBraun, H_2O and $O_2 <$ 0.1 ppm). The precursor mixture was prepared by arc-melting of strontium (Alfa Aesar, 99.95%) and silicon (Chempur, 99.999%) in the ratio 8:46 with 2.3% excess of strontium to compensate for evaporation loss. The resulting material was thoroughly ground and put into a BN crucible before being placed in a MgO octahedron (edge length 18 mm). High-pressure high-temperature synthesis was conducted in a multi-anvil Walker-type module[61] at 5(1) GPa and temperatures between 1273(127) and 1373(137) K before quenching under load. Calibration of pressure and temperature by resistance changes of bismuth and thermocouple-calibrated runs were realized prior to the experiments.

Phase assignment and determination of unit cell parameters was performed on basis of powder X-ray Guinier diffraction data (Cu $K_{\alpha 1}$ radiation, $\lambda = 1.540598$ Å, graphite monochromator, Huber 670 camera, $5^\circ \le 2\theta \le 100^\circ$, $\Delta 2\theta = 0.005^\circ$) at room temperature. Unit cell parameters were established from least squares refinement with LaB_6 (NIST) as an internal standard. Several single crystals were obtained by a treatment of the crude product with NaOH (1 mol L^{-1}) for one hour followed by washing with HCl (0.1 mol cl^{-1}) and ethanol. The size of the crystal chosen for the diffraction measurement amounted to $0.025 \times 0.030 \times 0.055$ mm^3. Single crystal X-ray diffraction was done with a Rigaku Saturn724+ diffractometer (2×2 bin mode, CCD detector, Mo K_α radiation, $\lambda = 0.71073$ Å). Absorption correction was realized by a multi-scan procedure (CrystalClear-SM Expert, Rigaku, 2011[62]). All crystallographic calculations were performed with the WinCSD program package.[63]

For metallographic analysis, the samples were polished by using disks with diamond powders (grain sizes 6, 3, and 0.25 μm) in paraffin. Energy-dispersive X-ray spectroscopy (EDXS) was performed with a Philips XL 30 scanning electron microscope (LaB_6 cathode) and an attached EDAX Si(Li) detector. Wavelength-dispersive X-ray

spectroscopy (WDXS) was conducted with a Cameca SX100 electron microprobe equipped with a tungsten cathode. $SrTiO_3$ and Si were selected as standards for Sr and Si, respectively. The analysis comprehended intensity measurements of the Sr-L_α and the Si-K_α lines. The X-ray emission lines were exited at an electron beam of 15 kV and a beam current of 100.00(1) nA for Sr and 10.00(1) nA for Si, respectively. The WDX spectrometer was equipped with PET (pentaerythritol) or TAP (thallium acid phthalate) monochromator crystals, the intensity of the Sr-L_α was collected simultaneously on two PET spectrometers. 20800 counts s^{-1} were measured for Si and 5400 counts s^{-1} for Sr, respectively.

Thin samples for transmission electron microscopy (TEM) study were obtained by the focused-ion-beam (FIB) lift-out technique[64] from a sample heated to 673 K and cooled to room temperature with a heating/cooling rate of 10 K min^{-1}. Thin cross-sections of micro-crystalline grains were extracted from a polished metallographic sample. In order to gain defined crystallographic oriented cross-sections, the cleavage habitus of the Sr_8Si_{46} crystallites was exploited. The FIB lift-out technique was conducted on a FEI Quanta 200 3D ion/electron dual beam device (FEI Company, Eindhoven, the Netherlands), which can be used both as a scanning electron microscope (SEM) and a scanning ion microscope (SIM). It is equipped with an OmniProbe micro-manipulator. First, protecting Pt layers (about 18 μm long, 2 μm thick, 2 μm high) were deposited on selected regions (parallel and perpendicular to the [010] and [110] axes of a crystallite using an acceleration voltage of 30 kV and a current of 0.1 nA. Each cross section (2 μm thickness) was prepared by applying a Ga-ion beam using an acceleration voltage of 30 kV and a current of 0.01–0.5 nA. The manufactured cut was transferred onto a copper OmniProbe TEM holder (Figure 2b) by using the in situ lift-out technique.[64] Finally, the cross-section was thinned to a thickness of about 60 nm by applying an acceleration voltage of 30 kV with currents of 0.5–0.01 nA of the Ga-ion beam. The thin crystalline FIB lamellas were used for selected area electron diffraction (SAED) and transmission electron microscopy (TEM) studies.

For high-resolution TEM, the sample was ground to fine powder and dispersed in isobutanol. The suspension was loaded on a 300-mesh copper grid covered with a holey carbon film (Plano GmbH, Wetzlar, Germany). After drying completely, electron diffraction was performed on a Tecnai F30 (FEI Thermofischer Technologies Inc., Hillsboro, OR, USA) with a field-emission gun at an acceleration voltage of 300 kV. The microscope is equipped with a slow-scan CCD camera (model MultiScan, 2K×2K pixels; Gatan Inc., Pleasanton, CA, USA). Spherical aberration corrected high-resolution TEM analyses of the sample were performed by the JEM-ARM300F (Grand ARM, JEOL, Akishima, Japan) with double correction. Dodecapole correctors in the beam and the image forming system correct the spherical aberration of the condenser and the objective lenses. TEM images were recorded on a 4K×4K pixel CCD array, model Gatan US4000 and analyzed with the DigitalMicrograph software (Gatan Inc., Pleasanton, CA, USA).

Chemical analysis for the determination of hydrogen, oxygen and nitrogen content was carried out through carrier gas hot extraction of samples, enclosed in tin capsules in a Leco TCH 600 device. The determined hydrogen content below 0.09% clearly eliminates any significant incorporation into the cage structure. Differential scanning calorimetry (DSC) experiments were performed in a Netzsch DSC 404C device (Netzsch-Gerätebau GmbH, Selb, Germany) by using corundum crucibles and heating and cooling rates of 10 K min^{-1} under argon atmosphere.

Nuclear magnetic resonance (NMR) experiments were performed with a Bruker Avance 500 spectrometer using a magnetic field of $B_0 = 11.74$ T and the standard Bruker MAS probe for 2.5 mm ZrO_2 rotors. The ^{29}Si signals were referenced to 1 vol.% TMS (tetramethylsilane) in $CDCl_3$ with the reference frequency of 99.3596 MHz. The spectra were obtained by the Hahn echo sequence with the duration of the first pulse of 1.8 μs and twice as long for the second one. The recovery time was 200 ms.

The measurement of the magnetic susceptibility was conducted using a polycrystalline sample of cylindrical shape (diameter 2.2 mm, length 1.0 mm) on a squid magnetometer (MPMS XL-7, Quantum Design) between 1.6 and 300 K in an external field of 2 mT. Electrical resistivity measurements were carried out in a temperature range from 1.8 to 300 K by using the van der Pauw method in the Quantum Design Physical Property Measurement System (PPMS 9) at fields between $\mu_0 H = 0$ to 9 T (contact geometry 0.20×0.40×0.40 mm). Heat capacity was measured from 0.4 to 10.1 K in magnetic fields up to 0.6 T in the Quantum Design Physical Property Measurement System.

For the electronic-band structure calculations, experimental values of lattice parameters and atomic coordinates are used. The TB-LMTO-ASA software[65] utilizes the Barth–Hedin exchange potential,[66] and the FPLO code[67] uses the GG approximation as parametrized by Perdew, Burke and Ernzerhof.[68]

To get the partial waves, the radial scalar-relativistic Dirac equation is solved. The calculation within the atomic sphere approximation (ASA) included sufficient corrections for the neglect of interstitial regions and partial waves of higher order.[69] For a self-consistent calculation, a basis set containing Sr(5s,4*d*) and Si(3s,3p) orbitals is employed with Sr(5p,4f) and Si(3d) functions being down-folded. The following radii of atomic spheres are used: $r(Sr1) = 2.460$ Å, $r(Sr2) = 2.638$ Å, $r(Si1) = 1.378$ Å, $r(Si2) = 1.397$ Å, $r(Si3) = 1.341$ Å. The electronic DOS is calculated by using the LMTO package using a mesh of 8×8×8K points.

The analysis of the chemical bonding in Sr_8Si_{46} is performed by the electron localizability approach in position space.[49] The electron localizability indicator (ELI) in its ELI-D representation[70,71] is calculated together with the electron density (ED), using specialized modules, which are implemented in the TB-LMTO-ASA and the FPLO program packages.[65,72] The results are the same irrespective of the employed computer code (see Supporting Information). Partial ELI-D contributions from different energy ranges in the electronic DOS are calculated with a dedicated procedure.[49] The topology of the three-dimensional distributions of ELI-D and ED was evaluated with the program DGrid.[73] Integration of the electron density in the basins bounded by zero-flux surfaces of the electron density or ELI-D gradient fields yield the atomic charges or bond populations, respectively. This procedure follows the quantum theory of atoms in molecules (QTAIM)[44]. Combined analysis of electron density and ELI-D yields basis information for the bonding situation in solids,[41,74,75] in particular for the intermetallic compounds.[76–78]

Acknowledgements

We thank Susann Leipe for supporting high-pressure syntheses. We express our gratitude to Marcus Schmidt and Susann Scharsach for DSC measurements, Ulrich Burkhardt, Sylvia Kostmann and Petra Scheppan for metallographic characterizations as well as Gudrun Auffermann and Ulrike Schmidt for chemical analysis. Useful discussions with Frank R. Wagner, Miroslav Kohout and Bodo Böhme are gratefully acknowledged. Financial support for J.-M.H. by the International Max Planck Re-

search School for Chemistry and Physics of Quantum Materials (IMPRS-CPQM) is gratefully recognized.

Conflict of interest

The authors declare no conflict of interest.

Keywords: chemical bonding · clathrate · high-pressure synthesis · silicon · strontium

[1] J.-T. Zhao, J. D. Corbett, *Inorg. Chem.* **1995**, *34*, 378 – 383.
[2] R. Nesper, *Prog. Solid State Chem.* **1990**, *20*, 1 – 45.
[3] J. M. Hübner, W. Carrillo-Cabrera, Yu. Prots, M. Bobnar, U. Schwarz, Yu. Grin, *Angew. Chem. Int. Ed.* **2019**, *58*, 12914 – 12918; *Angew. Chem.* **2019**, *131*, 13046 – 13050.
[4] H. Kawaji, H. Horie, S. Yamanaka, M. Ishikawa, *Phys. Rev. Lett.* **1995**, *74*, 1427 – 1429.
[5] J. L. Cohn, G. S. Nolas, V. Fessatidis, T. H. Metcalf, G. A. Slack, *Phys. Rev. Lett.* **1999**, *82*, 779 – 782.
[6] J. S. Kasper, P. Hagenmüller, M. Pouchard, C. Cros, *Science* **1965**, *150*, 1713 – 1714.
[7] J. Gallmeier, H. Schäfer, A. Weiss, *Z. Naturforsch. B* **1967**, *22*, 1080.
[8] C. Cros, M. Pouchard, P. Hagenmüller, J. S. Kasper, *Bull. Soc. Chim. Fr.* **1968**, 2737 – 2742.
[9] C. Cros, M. Pouchard, P. Hagenmüller, *J. Solid State Chem.* **1970**, *2*, 570 – 581.
[10] J. Gallmeier, H. Schäfer, A. Weiss, *Z. Naturforsch. B* **1969**, *24*, 665 – 667.
[11] S. Yamanaka, E. Enishi, H. Fukuoka, M. Yasukawa, *Inorg. Chem.* **2000**, *39*, 56 – 58.
[12] H. Fukuoka, J. Kiyoto, S. Yamanaka, *J. Solid State Chem.* **2003**, *175*, 237 – 244.
[13] H. Fukuoka, J. Kiyoto, S. Yamanaka, *Inorg. Chem.* **2003**, *42*, 2933 – 2937.
[14] Y. Liang, B. Böhme, M. Reibold, W. Schnelle, U. Schwarz, M. Baitinger, H. Lichte, Yu. Grin, *Inorg. Chem.* **2011**, *50*, 4523 – 4528.
[15] R. Castillo, W. Schnelle, M. Bobnar, U. Burkhardt, B. Böhme, M. Baitinger, U. Schwarz, Yu. Grin, *Z. Anorg. Allg. Chem.* **2015**, *641*, 206 – 213.
[16] A. Kitano, K. Moriguchi, M. Yonemura, S. Munetoh, A. Shintani, H. Fukuoka, S. Yamanaka, E. Nishibori, M. Takata, M. Sakata, *Phys. Rev. B* **2001**, *64*, 045206.
[17] B. Liu, X. Jia, H. Sun, B. Sun, Y. Zhang, H. Liu, L. Kong, D. Huo, H. J. Ma, *J. Solid State Chem.* **2016**, *233*, 363 – 367.
[18] B. Böhme, A. Guloy, Z. Tang, W. Schnelle, U. Burkardt, M. Baitinger, Yu. Grin, *J. Am. Chem. Soc.* **2007**, *129*, 5348 – 5349.
[19] G. K. Ramachandran, J. Dong, J. Diefenbacher, J. Gryko, R. F. Marzke, O. F. Sankey, P. F. McMillan, *J. Solid State Chem.* **1999**, *145*, 716 – 730.
[20] S. Stefanoski, G. S. Nolas, *Cryst. Growth Des.* **2011**, *11*, 4533 – 4537.
[21] G. K. Ramachandran, P. F. McMillan, J. Dong, O. F. Sankey, *J. Solid State Chem.* **2000**, *154*, 626 – 634.
[22] A. Wosylus, I. Veremchuk, W. Schnelle, M. Baitinger, U. Schwarz, Yu. Grin, *Chem. Eur. J.* **2009**, *15*, 5901 – 5903.
[23] I. Veremchuk, A. Wosylus, B. Böhme, M. Baitinger, H. Borrmann, Yu. Prots, U. Burkhardt, U. Schwarz, Yu. Grin, *Z. Anorg. Allg. Chem.* **2011**, *637*, 1281 – 1286.
[24] H. G. von Schnering, J. Llanos, K. Peters, M. Baitinger, Yu. Grin, R. Nesper, *Z. Kristallogr. New Cryst. Struct.* **2011**, *226*, 9 – 10.
[25] B. Eisenmann, H. Schäfer, R. Zagler, *J. Less-Common Met.* **1986**, *118*, 43 – 55.
[26] G. Cordier, P. Woll, *J. Less-Common Met.* **1991**, *169*, 291 – 302.
[27] N. Nasir, A. Grytsiv, N. Melnychenko-Koblyuk, P. Rogl, E. Bauer, R. Lackner, E. Royanian, G. Giester, A. Saccone, *J. Phys. Condens. Matter* **2009**, *21*, 385404.
[28] W. Jung, H. Kessens, A. Ormeci, W. Schnelle, U. Burkhardt, H. Borrmann, H. D. Nguyen, M. Baitinger, Yu. Grin, *Dalton Trans.* **2012**, *41*, 13960 – 13968.
[29] W. Carrillo-Cabrera, J. Curda, H. G. von Schnering, K. Peters, S. Paschen, M. Baenitz, Yu. Grin, *Z. Kristallogr. New Cryst. Struct.* **2000**, *215*, 321 – 322.
[30] P. Toulemonde, C. Adessi, X. Blase, A. San Miguel, J. L. Tholence, *Phys. Rev. B* **2005**, *71*, 094504.
[31] J. H. Roudebush, N. Tsujii, A. Hurtando, H. Hope, Yu. Grin, S. M. Kauzlarich, *Inorg. Chem.* **2012**, *51*, 4161 – 4169.
[32] W. Carrillo-Cabrera, R. Cardoso Gil, Yu. Grin, *Z. Kristallogr. New Cryst. Struct.* **2002**, *217*, 179 – 180.
[33] M. Imai, T. Kikegawa, *Inorg. Chem.* **2008**, *47*, 8881 – 8883.
[34] Y. Imai, A. Watanabe, *Intermetallics* **2010**, *18*, 542 – 547.
[35] P. Norouzzadeh, J. S. Krasinski, C. W. Myles, D. Vashaee, *Phys. Chem. Chem. Phys.* **2015**, *17*, 8850 – 8859.
[36] J. Evers, G. Oehlinger, A. Weiss, *J. Solid State Chem.* **1977**, *20*, 173 – 181.
[37] B. N. Dutta, *Phys. Status Solidi B* **1962**, *2*, 984 – 987.
[38] M. Beekman, M. Baitinger, H. Borrmann, W. Schnelle, K. Meier, G. S. Nolas, Yu. Grin, *J. Am. Chem. Soc.* **2009**, *131*, 9642 – 9643.
[39] J. He, D. D. Klug, K. Uehara, K. F. Preston, C. I. Ratcliffe, J. S. Tse, *J. Phys. Chem. B* **2001**, *105*, 3475 – 3485.
[40] J. Emsley, *The Elements*, Clarendon, Oxford, **1991**.
[41] Yu. Grin, in *Comprehensive Inorganic Chemistry II, Vol. 2*, Elsevier, Oxford, **2013**, pp. 359 – 373.
[42] A. Bhattacharya, C. Carbogno, B. Böhme, M. Baitinger, Yu. Grin, M. Scheffler, *Phys. Rev. Lett.* **2017**, *118*, 236401..
[43] A. Ormeci, Yu. Grin, *J. Thermoelectr.* **2015**, *6*, 16 – 32.
[44] R. F. W. Bader, *Atoms in Molecules: A Quantum Theory*, Oxford University Press, Oxford **1999**.
[45] U. Schwarz, R. Castillo, A. Wosylus, L. Akselrud, Yu. Prots, B. Wahl, T. Doert, M. Bobnar, Yu. Grin, *Z. Naturforsch. B* **2019**, *74*, 137 – 145.
[46] X.-J. Feng, Yu. Prots, M. Bobnar, M. P. Schmidt, W. Schnelle, J.-T. Zhao, Yu. Grin, *Chem. Eur. J.* **2015**, *21*, 14471 – 14477.
[47] A. Palasyuk, Yu. Grin, G. J. Miller, *J. Am. Chem. Soc.* **2014**, *136*, 3108 – 3117.
[48] X.-J. Feng, Yu. Prots, M. P. Schmidt, S. Hoffmann, I. Veremchuk, W. Schnelle, U. Burkhardt, J.-T. Zhao, Yu. Grin, *Inorg. Chem.* **2013**, *52*, 8971 – 8978.
[49] F. R. Wagner, V. Bezugly, M. Kohout, Yu. Grin, *Chem. Eur. J.* **2007**, *13*, 5724 – 5741.
[50] C. Börrnert, Yu. Grin, F. R. Wagner, *Z. Anorg. Allg. Chem.* **2013**, *639*, 2013 – 2024.
[51] S. Stefanoski, C. D. Malliakas, M. G. Kanatzidis, G. S. Nolas, *Inorg. Chem.* **2012**, *51*, 8686 – 8692.
[52] S. Stefanoski, J. Martin, G. S. Nolas, *J. Phys. Condens. Matter* **2010**, *22*, 485404.
[53] S. Stefanoski, M. Beekman, W. Wong-Ng, P. Zavalij, G. S. Nolas, *Chem. Mater.* **2011**, *23*, 1491 – 1495.
[54] R. Demchyna, U. Köhler, Yu. Prots, W. Schnelle, M. Baenitz, U. Burkhardt, S. Paschen, U. Schwarz, *Z. Anorg. Allg. Chem.* **2006**, *632*, 73 – 78.
[55] M. Tinkham, *Introduction to Superconductivity.* McGraw – Hill, New York, **1996**.
[56] C. Kittel, *Introduction to Solid State Physics*, Wiley, New York **2005**.
[57] E. Grüneisen, *Ann. Phys.* **1933**, *408*, 530 – 540.
[58] R. Lortz, R. Viennois, A. Petrovic, Y.-X. Wang, P. Toulemonde, C. Meingast, M. M. Koza, H. Mutka, A. Bossak, A. San Miguel, *Phys. Rev. B* **2008**, *77*, 224507.
[59] W. L. McMillan, *Phys. Rev.* **1968**, *167*, 331 – 344.
[60] N. R. Werthamer, E. Helfand, P. C. Hohenberg, *Phys. Rev.* **1966**, *147*, 295 – 302.
[61] D. Walker, M. A. Carpenter, C. M. Hitch, *Am. Mineral.* **1990**, *75*, 1020 – 1028.
[62] Rigaku Americas and Rigaku. *CrystalClear-SM Expert.* **2011**, Rigaku Americas, The Woodlands, Texas, USA, and Rigaku Corporation, Tokyo, Japan.
[63] L. Akselrud, Yu. Grin, *J. Appl. Crystallogr.* **2014**, *47*, 803 – 805.
[64] Z. Wang, W. Wan, J. Sun, W. Carrillo-Cabrera, D. Grüner, X. Yin, S. Qiu, G. Zhu, X. Zou, *CrystEngComm* **2012**, *14*, 2204 – 2212.
[65] O. Jepsen, A. Burkhardt, O. K. Andersen, The Program TB-LMTO-ASA. Version 4.7. Max-Planck-Institut für Festkörperforschung, Stuttgart, **1999**.
[66] U. von Barth, L. Hedin, *J. Phys. Sect. C* **1972**, *5*, 1629 – 1642.
[67] K. Koepernik, H. Eschrig, *Phys. Rev. B* **1999**, *59*, 1743 – 1757.
[68] J. P. Perdew, K. Burke, M. Ernzerhof, *Phys. Rev. Lett.* **1996**, *77*, 3865 – 3868.
[69] O. K. Andersen, *Phys. Rev. B* **1975**, *12*, 3060 – 3083.
[70] M. Kohout, *Int. J. Quantum Chem.* **2004**, *97*, 651 – 658.

[71] M. Kohout, *Faraday Discuss.* **2007**, *135*, 43 – 54.
[72] A. Ormeci, H. Rosner, F. R. Wagner, *J. Phys. Chem. A* **2006**, *110*, 1100 – 1105.
[73] M. Kohout, DGrid, versions 4.6 – 5.0, **2018**.
[74] M. Kohout, A. Savin, *Int. J. Quantum Chem.* **1996**, *60*, 875 – 882.
[75] Yu. Grin, A. Savin, B. Silvi, in *The Chemical Bond: Fundamental Aspects of Chemical Bonding* (Eds.: G. Frenking, S. Shaik), Wiley-VCH, Weinheim, **2014**, pp. 345 – 382.
[76] D. Bende, F. R. Wagner, Yu. Grin, *Inorg. Chem.* **2015**, *54*, 3970 – 3978.
[77] F. R. Wagner, R. Cardoso-Gil, B. Boucher, M. Wagner-Reetz, J. Sichelschmidt, P. Gille, M. Baenitz, Yu. Grin, *Inorg. Chem.* **2018**, *57*, 12908 – 12919.
[78] R. Freccero, P. Solokha, S. De Negri, A. Saccone, Yu. Grin, F. R. Wagner, *Chem. Eur. J.* **2019**, *25*, 6600 – 6612.

Manuscript received: September 10, 2019
Revised manuscript received: October 23, 2019
Accepted manuscript online: October 25, 2019
Version of record online: December 12, 2019

